Elucidating the Mesoscale Deformation in a Multi-Principle Element Alloy with Hexagonal Closed-Packed Crystal Structure

Jie Kuang[a], Dongdong Zhang[b], Shubin Wang[c], Qinghuan Huo[d], Xinpeng Du[e], Yuqing Zhang[a], Gang Liu[a,*], Wei Wen[f,*], Jinyu Zhang [a], Jun Sun[a,*]

a) State Key Laboratory for Mechanical Behavior of Materials, Xi'an Jiaotong University, Xi'an 710049, P.R. China
b) Department of Industrial and Systems Engineering, The Hong Kong Polytechnic University, Hong Kong 999077, P.R. China
c) Shanghai Key Lab of Advanced High-temperature Materials and Precision Forming, School of Materials Science and Engineering, Shanghai Jiao Tong University, Shanghai, 200240, P.R. China
d) School of Materials Science and Engineering, Central South University, Changsha, 410083, P.R. China
e) The College of Optics & Photonics, University of Central Florida, Orlando, FL 32826, USA
f) School of Engineering, Lancaster University, Lancaster, LA1 4YW, UK

Corresponding authors:

Gang Liu: lgsammer@ xjtu.edu.cn

Wei Wen: w.wen2@lancaster.ac.uk

Jun Sun: junsun@ xjtu.edu.cn

Abstract

To date, the exploration of multi-principal element alloys (MPEAs) has rarely ventured into the realm of hexagonal close-packed (HCP) structures. In this research, we embarked on a pioneering systematic comparison between a single-phase Ti-Zr-Hf HCP-MPEA and Ti regarding their dislocation activities and mesoscale deformation homogeneity. Through large-area high-resolution quasi-in-situ slip trace analysis and crystal plasticity finite element modeling, we identified HCP-MPEA's significantly enhanced pyramidal slip activities—resulted from minimized disparities among different deformation modes—notably improve the material's intragranular deformation homogeneity. Alongside MPEA's intrinsically high slip resistance, it renders HCP-MPEA an outstanding strength-toughness combination relative to its conventional HCP counterparts.

Keywords multi-principle element alloys; hexagonal-close packed structure; slip activity; crystal plasticity; deformation homogeneity

Introduction

Metals and alloys are widely recognized as the major workhorse materials for the manufactory industry and structural applications [1]. Unlike conventional metallic materials which are normally developed based on a single host metal, multi-principle element alloys (MPEAs), first proposed by Yeh et al. [2], stand out by consisting of constituent elements with near-equal atomic fractions. With compositions in the unexplored middle section of the phase diagram, MPEAs challenge the classic concept of solute and solvent, exhibiting unique properties including concentration fluctuation/undulation [3,4], spatially variable stacking fault energy (SFE) [5,6], rough/wavy dislocation morphology [5,7], jerky and sluggish dislocation motion [8,9], etc. These characteristics have been shown to introduce significant challenges when attempting to comprehend/evaluate the deformation behavior of MPEAs using prior microstructure-property knowledge, impeding the development of novel MPEAs [10]. Accordingly, a growing number of researchers in the MPEA community are shifting

their focus from exploring new alloy compositions (which has been a longstanding emphasis) to bridging the gap between the distinctive dislocation behaviors and the microstructural features inherent to MPEAs [11]. For example, Ding et al. [3] found the existence of concentration wave in CrFeCoNiPd and this phenomenon could improve the strength-ductility balance of the material. Smith et al. [12] discovered that the rugged energy landscape in MPEAs increased the critical stress for activating the Frank-Read source, resulting in "cocktail hardening". Lei et al. [13] reported the formation of ordered interstitial complexes in oxygen-doped TiZrHfNb alloys led to enhanced cross-slip activities and improved mechanical properties.

It is worth noting that while there have been studies on similar topics on other MPEA systems (compositionally), the overwhelming majority of the existing publications have focused on MPEAs with either face-center cubic (FCC) [14-16] or body-center cubic (BCC) structures [7,17] (or occasionally FCC/BCC dual-phase structures [18-21]). The hexagonal close-packed (HCP) structure, though being referred to by physical metallurgy textbooks as another cornerstone structure in metallic materials alongside FCC and BCC, has been largely overlooked in the research field of MPEAs. To date, very few HCP MPEAs have been reported, and even less are comprehensive studies on their deformation mechanisms [22-24]. Therefore, filling this glaring hole and answering the question as to what sets HCP MPEAs apart from conventional HCP metals/alloys, particularly in terms of their plastic deformation mechanisms, have become a growing interest. This interest has recently been fueled by Li et al. [25,26] and Bu et al.'s [27], who suggest the incorporation of an HCP phase into an FCC matrix as a potential route to advancing the next-generation MPEAs with superior mechanical performances. In fact, our previous research [28] demonstrates that the model Ti-Zr-Hf HCP MPEA, though possessing a simple single-phase coarse-grained microstructure, surpasses all existing (quasi-)single-phase HCP alloys in strength-toughness performance, and even rivals most of those with delicately designed microstructures including nanostructures and heterostructures (Fig. S1). At the nano and micro scale, we discovered that the intrinsic characteristics of MPEAs—namely,

high alloy concentration and local fluctuation—significantly enhance the activity of pyramidal slips in comparison to conventional HCP alloys. Yet, what remains unexplored is the link between this unique dislocation activity and mesoscale deformation phenomena, such as stress/strain distribution during deformation—especially near grain boundaries, which is the most critical factor that determines the mechanical properties of single-phase coarse-grained alloys [29-32]. This gap limits the potential for targeted microstructure and texture optimization to further enhance material performance.

In this work, a Ti-Zr-Hf MPEA with single-phase HCP structure and c/a ratio approximately equal to pure Ti were prepared. By employing large-area high-resolution quasi-in-situ slip trace analysis and crystal plasticity finite element modeling (CPFEM), we conducted a comparative investigation of dislocation and twinning activities between Ti-Zr-Hf MPEAs and pure Ti. This comparison allowed us to illuminate, for the first time, the link between dislocation/twinning activity and mesoscale deformation behaviors in HCP MPEAs, thereby deciphering the origin of the HCP MPEA's outstanding strength-toughness combination compared to traditional HCP counterparts. The findings are expected to have implications for the advancement of not only single-phase HCP MPEAs but also those featuring a dual-phase combination of FCC (or BCC) and HCP structures.

Materials and methods

The MPEA ingots used in this work were prepared by arc-melting, and has a composition of Ti : Zr : Hf = 1.2 : 1 : 1 (atomic ratio, denoted as HCP-MPEA hereafter). The two materials underwent different cold rolling and annealing schemes to obtain comparable single-phase microstructure and texture. Uniaxial tension and compression tests were conducted to characterize the material's mechanical behavior at room temperature. Quasi-in-situ slip trace analysis based on scanning electron microscope (SEM) and electron backscattered diffraction (EBSD) technique were carried out to acquire statistical data on the active slip systems as did in our prior work [33-35] and

other studies [32,36-43]. CPFEM was performed in the PRISMS-Plasticity framework [44] to understand slip activity and meso-scale stress/strain localization. For detailed descriptions of the experimental and simulation procedures, readers are referred to the Supplementary Materials and our previous publications [16,18,19,28,33,45-47].

Results and discussion

The microstructural analysis of the as-cast HCP-MPEA, depicted in Fig. S2, indicates a homogeneous single-phase HCP structure without noticeable elemental segregation, and a c/a ratio of approximately 1.586, closely matching that of pure Ti at 1.587. Fig. 1(a) and (b) shows the microstructure and texture of the HCP-MPEA and pure Ti following cold rolling and recrystallization annealing. Thanks to the meticulously chosen thermomechanical processing parameters (Please see the Supplementary Materials), both samples present a grain size distribution that follows a Gaussian pattern with mean size ranging between 20~30 μm. Besides, both materials display a basal texture with peak intensities (~8 multiple random distribution (MRD)), located near the sheet normal direction (ND) and spread towards the rolling direction (RD). These factors ensure that effects from the crystal structure, microstructure, and texture on mechanical properties are minimized, which therefore lays the foundation of the present research that focuses on comparing the impacts of slip/twinning activities.

To capture the macroscopic mechanical response using crystal plasticity, CPFEM was first conducted on an aggregate of 1000 single crystals, each modeled by a single eight-node linear hexahedral element, as depicted in Fig. 2(a). Fig. 2(b) displays the CPFEM input textures discretized from the experimental texture of HCP-MPEA and Ti. As can be seen, the discretized texture closely resembles the corresponding measured ones (Fig. 1(c)), albeit with marginally higher peak intensities. Tables 1 and 2 present the optimized critical resolved shear stress (CRSS) and hardening parameters for various slip modes in Ti and HCP-MPEA, respectively. These parameters were chosen to achieve the closest match between the experimental and CPFEM stress-strain responses in both tension and compression, as shown in Fig. 2(c). A notable observation

from these tables is that the HCP-MPEA demonstrates significantly higher CRSS values compared to Ti, alongside a marked reduction in the CRSS disparities among different deformation modes. In fact, despite CPFEM's success in replicating experimental stress-strain curves, the inherent underdetermined nature of the parameter optimization process in CPFEM means multiple sets of parameters could potentially fit the same data, raising concerns about the authenticity of the modeled deformation mechanisms. To mitigate these concerns, Fig. 2(d) provides a direct comparison of twin volume fraction evolution between experimental data and simulation results—performed without any fitting or tweaking. As can be seen, the evolution of twin volume fraction in both materials can be well-tracked by the model using the parameters in Table 1 and 2, confirming the parameters' validity and the model's capability to authentically reflect the complex interplay of mechanisms in the two materials that govern not only their mechanical responses but also the microstructural changes.

Building on the validated parameters listed in Tables 1 and 2, we expanded our modeling to investigate the mesoscale deformation behaviors, facilitating direct comparisons with high-resolution quasi-in-situ slip trace observations. One example of the quasi-in-situ slip trace analysis procedure is provided in Fig. 3. For more information of this method readers are referred to Supplementary Materials. Fig. 4 compares the results from slip trace analysis and CPFEM for a selected representative region in the HCP-MPEA quasi-in-situ sample. Fig. 4(a) and (b) are the microstructure of the region and the corresponding finite element (FE) mesh, respectively, prior to tension. After a true plastic strain of ~0.08, the surface morphology and the spatial distribution of the slip activity are given in Fig. 4(c) and Fig. 4(d1~3) respectively. It can be seen that the grain-level slip activities are well replicated by the CPFEM: nearly all grains with identified first order pyramidal (Pyr1) slip traces align with grains that exhibit high activity of either Pyr1 <a> or Pyr1 <c+a> (or both) in CPFEM. For statistical sufficiency, Fig. 4(e) displays a comparison on the statistics of slip trace results and the normalized shear of the dislocations (i.e. total shear divided by the norm of Burgers vector) obtained by CPFEM. Obviously, the experiment and CPFEM are in

qualitative agreement, both showing dislocations on Pyr1 planes are notably more active in HCP-MPEA than in Ti, contrasting with the lesser activity on prismatic (Prism) planes. The slip activity evolution with strain predicted by CPFEM (Fig. 4(f)) further pinpoints that the enhanced dislocation activities in HCP-MPEA on Pyr1 plane stem not only from the Pyr1<c+a> slip mode but also from the Pyr1<a> slip mode (the enhancement of the latter is actually even more pronounced). This concurs with the reduced CRSS gap in HCP-MPEA between the two Pyr1 slip modes and the prism <a> slip mode, as illustrated in Table 1 and 2. It agrees as well with our prior first-principle calculations and dislocation density measurement [28], which show that the Peierls stress ratio between non-Prism dislocations and Prism <a> dislocations are significantly reduced by the high alloy concentration and local fluctuation intrinsic to HCP-MPEAs, giving rise to the enhanced activity of Pyr1 <a> and Pyr1 <c+a>, and thus resulting in a higher <c+a> dislocation proportion in the HCP-MPEA than in the Ti. In this sense, the present CPFEM faithfully reproduces not only the macroscopic mechanical behavior of HCP-MPEA and Ti, but also their mesoscale distribution of slip activities. Therefore, it underpins the subsequent application of the model to examine mesoscale stress-strain distributions and their implications for mechanical properties.

To eliminate the influence of microstructure and texture, CPFEM for both HCP-MPEA and Ti was conducted using identical 'virtual' microstructures (Fig. 5(a) and (b)) but with material-specific CRSS and hardening parameters from Table 1 and 2. The results reveal that despite sharing the same microstructure, Ti is more susceptible to stress (indicated by red arrows in Fig. 5(c1~c2)) and strain concentration (highlighted by the green arrows in Fig. 5(d1~d2) and the line profile in Supplementary Materials). Fig. 5(e) and (f) offer a quantitative comparison of the normalized Von Mises stress (local Von Mises stress divided by the macroscopic stress) distribution and the normalized Von Mises strain (local Von Mises strain divided by the macroscopic strain) distribution in HCP-MPEA versus Ti. In Fig. 5(e), HCP-MPEA shows a sharp peak at unity, whereas Ti features not only a broader main peak around the same value but also an additional minor peak at ~1.5. This indicates that Ti experiences more extensive

stress concentration, with a considerable fraction of the material subjected to local stresses approximately 1.5 times the macroscopic Von Mises stress. A similar, albeit less pronounced, pattern is observed in Fig. 5(f). Here, Ti has a higher proportion of areas with local strains deviating wildly (towards both higher end and lower end) from the macroscopic strain, indicating more widespread strain localization compared to HCP-MPEA.

The reduced stress/strain concentration in the single-phase HCP-MPEA should arise from the enhanced intergranular strain compatibility within the material, which is usually believed to be controlled by the slip transfer [31,36,39,48,49]. Typically, the likelihood of slip transfer is determined by the Luster-Morris factor m', which is defined as $m' = \cos\psi \cos\kappa$, where ψ is the angle between slip plane normal directions, κ is the angle between slip directions [48,50]. A higher m' value signifies better alignment of slip systems across grain boundaries, facilitating slip transfer [51,52]. Since effective slip transfer can mitigate stress/strain concentration [51], the more profuse the slip transfer, the better the intergranular compatibility [36]. However, what initially perplexes us is that despite HCP-MPEA and Ti displaying similar m' distributions (due to their nearly identical misorientation distribution functions, see Fig. S5), Ti exhibits significantly more slip transfer events than HCP-MPEA does. Moreover, although Ti shows a higher frequency of slip transfer, it paradoxically demonstrates a more heterogeneous stress/strain distribution, marked by more pronounced stress/strain localizations near grain boundaries and triple junctions. These phenomena highlight two critical insights into the differing strain accommodation pattern of the two materials: (1) the occurrence of slip transfer in HCP-MPEA does not seem to be dictated solely by geometrical considerations such as m', unlike in Ti where the m' criterion predicts slip transfer event more accurately; and (2) the strain incompatibility in HCP-MPEA appears to be mitigated through mechanisms other than intergranular accommodation, which, in contrast, plays a significant role in the ductility of Ti.

The first observation corroborates findings from multiple studies emphasizing the need to incorporate additional factors, such as the Schmid factor, into slip transfer

criteria [31,40,53]. In fact, in one of our previous publications [28], we introduced a slip transfer probability criterion that takes into account grain orientation, grain boundary misorientation, grain boundary strength, and CRSS. Following this methodology and applying the optimized CRSS values outlined in Tables 1 and 2, we calculated the slip transfer probability for both Ti and HCP-MPEA. (readers are referred to Supplementary Materials for the detailed calculation process). Unlike the m' values, which are geometrically identical for both materials as shown in Fig. 5(h), the slip transfer probability—incorporating physical properties such as CRSS—provides a plausible qualitative rationale for the observed differences in slip transfer frequency between Ti and HCP-MPEA, as depicted in Fig. 5(i). This indicates that the influence of grain boundary strength and CRSS account for the significantly lower propensity for slip transfer in HCP-MPEA compared to Ti.

As for the second point, the need to keep deformation continuity requires strain accommodation, achieved through either intergranular or intragranular mechanisms. Ti exhibits a large CRSS gap between its soft and hard deformation modes. To accommodate the resulting strain incompatibilities, deformation must be managed at the grain boundaries, necessitating extensive slip transfer. While this may aid intergranular strain accommodation and improve ductility [41,45], it leads to a reduced Hall-Petch slope and less effective grain boundary strengthening [43]. Coupled with the inherently low CRSS of pure metals, this results in a good ductility but a rather low strength in Ti, which is unfavorable to strength-toughness combination. In contrast to Ti, first principle calculations [28] and CPFEM results (Table 1 and 2) both demonstrate that the HCP-MPEA has a narrow gap of slip resistance between hard and soft deformation modes. This leads to a more uniform distribution of slip activities across all slip systems, which enhances the intragranular strain compatibility. Consequently, HCP-MPEA demonstrates less dependence on grain boundary mechanisms, such as slip transfer and grain boundary sliding (GBS), for achieving strain accommodation. This is evidenced by the scarce occurrence of slip transfer events. The alleviated reliance on grain boundaries for strain accommodation, combined with the substantial CRSS

increase afforded by solution strengthening inherent to all MPEAs, should be the underlying reason for the HCP-MPEA's exceptional strength-toughness combination (Fig. S1).

Summary and conclusions

Unlike pure Ti, which depends on widespread slip transfer at grain boundaries to manage strain incompatibilities—resulting in low strength but high ductility—the HCP-MPEA achieves an outstanding strength-toughness combination through its intrinsically high slip resistance and a more uniform pattern of intragranular deformation. The former bolsters strength, whereas the latter curtails the occurrence of significant stress localizations at grain boundaries and triple junctions. The underlying mechanism for this improved mesoscale deformation homogeneity is the enhanced activity of dislocations on pyramidal planes, facilitated by the reduced CRSS disparities among different slip modes. The elevated pyramidal slip activity renders the grains in HCP-MPEA "self-compatible" and thus become less dependent on grain boundary mechanisms such as slip transfer for the purpose of strain accommodation

Acknowledgement

This work was supported by the National Natural Science Foundation of China (Nos. 52371119, U23A6013, 92360301, U2330203, 51801147, 51790482), the National Key Research and Development Program of China (No. 2017YFB0702301), and Shaanxi Province Innovation Team Project (No. 2024RS-CXTD-58). Dr. Fuxue Yan and Mr. Yuhui Wan are acknowledged for their help with the electron microscopes. Besides, the authors would like to express their gratitude to Dr. Yaghoobi and Dr. Depriester for their kind suggestions on the modeling. The editors and reviewers are also acknowledged, for their comments and suggestions that help us improve the quality of the manuscript.

Reference

1. Lu K. Materials science. The future of metals. Science. 2010 Apr 16;328(5976):319-20.
2. Yeh JW, Chen SK, Lin SJ, et al. Nanostructured high‐entropy alloys with multiple principal elements: novel alloy design concepts and outcomes. Advanced engineering materials. 2004;6(5):299-303.
3. Ding Q, Zhang Y, Chen X, et al. Tuning element distribution, structure and properties by composition in high-entropy alloys. Nature. 2019 Oct;574(7777):223-227.
4. Bu Y, Wu Y, Lei Z, et al. Local chemical fluctuation mediated ductility in body-centered-cubic high-entropy alloys. Materials Today. 2021.
5. Li QJ, Sheng H, Ma E. Strengthening in multi-principal element alloys with local-chemical-order roughened dislocation pathways. Nat Commun. 2019 Aug 8;10(1):3563.
6. Xu XD, Liu P, Tang Z, et al. Transmission electron microscopy characterization of dislocation structure in a face-centered cubic high-entropy alloy Al0.1CoCrFeNi. Acta Materialia. 2018;144:107-115.
7. Wang F, Balbus GH, Xu S, et al. Multiplicity of dislocation pathways in a refractory multiprincipal element alloy. Science. 2020;370(6512):95-101.
8. Utt D, Lee S, Xing Y, et al. The origin of jerky dislocation motion in high-entropy alloys. Nat Commun. 2022 Aug 15;13(1):4777.
9. Li W, Lyu S, Chen Y, et al. Fluctuations in local shear-fault energy produce unique and dominating strengthening in metastable complex concentrated alloys. Proc Natl Acad Sci U S A. 2023 Mar 21;120(12):e2209188120.
10. Wu Y, Zhang F, Yuan X, et al. Short-range ordering and its effects on mechanical properties of high-entropy alloys. Journal of Materials Science & Technology. 2021;62:214-220.
11. Ma E. Unusual dislocation behavior in high-entropy alloys. Scripta Materialia. 2020;181:127-133.
12. Smith LTW, Su Y, Xu S, et al. The effect of local chemical ordering on Frank-Read source activation in a refractory multi-principal element alloy. International Journal of Plasticity. 2020;134:102850.
13. Lei Z, Liu X, Wu Y, et al. Enhanced strength and ductility in a high-entropy alloy via ordered oxygen complexes. Nature. 2018 Nov;563(7732):546-550.
14. Yin B, Yoshida S, Tsuji N, et al. Yield strength and misfit volumes of NiCoCr and implications for short-range-order. Nat Commun. 2020 May 19;11(1):2507.
15. Chen X, Wang Q, Cheng Z, et al. Direct observation of chemical short-range order in a medium-entropy alloy. Nature. 2021 Apr;592(7856):712-716.
16. Zhang DD, Zhang JY, Kuang J, et al. Superior strength-ductility synergy and strain hardenability of Al/Ta co-doped NiCoCr twinned medium entropy alloy for cryogenic applications. Acta Materialia. 2021;220:117288.
17. Chen B, Li S, Zong H, et al. Unusual activated processes controlling dislocation motion in body-centered-cubic high-entropy alloys. Proceedings of the National Academy of Sciences. 2020;117(28):16199-16206.
18. Zhang DD, Zhang JY, Kuang J, et al. Low modulus-yet-hard, deformable multicomponent fibrous B2-phase making a medium-entropy alloy ultra-strong and ductile. Scripta Materialia. 2023;222:115058.

19. Zhang D, Zhang J, Kuang J, et al. The B2 phase-driven microstructural heterogeneities and twinning enable ultrahigh cryogenic strength and large ductility in NiCoCr-based medium-entropy alloy. Acta Materialia. 2022;233:117981.
20. Nguyen NT-C, Asghari-Rad P, Zargaran A, et al. Relation of phase fraction to superplastic behavior of multi-principal element alloy with a multi-phase structure. Scripta Materialia. 2022;221:114949.
21. Bai Y, Zhang K, Chen T, et al. Alterable tension-compression asymmetry in work hardening of an additively manufactured dual-phase high-entropy alloy. International Journal of Plasticity. 2022;158:103432.
22. Takeuchi A, Wada T, Kato H. High-Entropy Alloys with Hexagonal Close-Packed Structure in Ir₂₆Mo₂₀Rh_{22.5}Ru₂₀W_{11.5} and Ir_{25.5}Mo₂₀Rh₂₀Ru₂₅W_{9.5} Alloys Designed by Sandwich Strategy for the Valence Electron Concentration of Constituent Elements in the Periodic Chart. Materials Transactions. 2019;60(8):1666-1673.
23. Rogal L, Bobrowski P, Kormann F, et al. Computationally-driven engineering of sublattice ordering in a hexagonal AlHfScTiZr high entropy alloy. Sci Rep. 2017 May 19;7(1):2209.
24. Feuerbacher M, Heidelmann M, Thomas C. Hexagonal High-entropy Alloys. Materials Research Letters. 2014;3(1):1-6.
25. Li Z, Pradeep KG, Deng Y, et al. Metastable high-entropy dual-phase alloys overcome the strength-ductility trade-off. Nature. 2016 Jun 9;534(7606):227-30.
26. Li Z, Tasan CC, Pradeep KG, et al. A TRIP-assisted dual-phase high-entropy alloy: Grain size and phase fraction effects on deformation behavior. Acta Materialia. 2017;131:323-335.
27. Bu Y, Li Z, Liu J, et al. Nonbasal Slip Systems Enable a Strong and Ductile Hexagonal-Close-Packed High-Entropy Phase. Phys Rev Lett. 2019 Feb 22;122(7):075502.
28. Kuang J, Zhang D, Zhang Y, et al. Achieving excellent strength-toughness combination in hexagonal closed-packed multi-principle element alloys via 〈c + a〉 slip promotion. Scripta Materialia. 2024;242:115903.
29. Bieler TR, Eisenlohr P, Roters F, et al. The role of heterogeneous deformation on damage nucleation at grain boundaries in single phase metals. International Journal of Plasticity. 2009;25(9):1655-1683.
30. Zeng ZR, Bian MZ, Xu SW, et al. Effects of dilute additions of Zn and Ca on ductility of magnesium alloy sheet. Materials Science and Engineering: A. 2016;674:459-471.
31. Sun J, Jin L, Dong J, et al. Towards high ductility in magnesium alloys - The role of intergranular deformation. International Journal of Plasticity. 2019;123:121-132.
32. Wang H, Boehlert CJ, Wang QD, et al. In-situ analysis of the tensile deformation modes and anisotropy of extruded Mg-10Gd-3Y-0.5Zr (wt.%) at elevated temperatures. International Journal of Plasticity. 2016;84:255-276.
33. Kuang J, Zhao X, Du X, et al. Ductilizing Al-Mn strips via gradient texture. Materials Research Letters. 2023;11(6):430-438.
34. Kuang J, Du X, Li X, et al. Athermal influence of pulsed electric current on the twinning behavior of Mg–3Al–1Zn alloy during rolling. Scripta Materialia. 2016;114:151-155.
35. Kuang J, Zhang Y, Du X, et al. On the strengthening and slip activity of Mg-3Al-1Zn alloy with pre-induced {101¯2} twins. Journal of Magnesium and Alloys. 2021.

36. Wang T, Zha M, Du C, et al. High strength and high ductility achieved in a heterogeneous lamella-structured magnesium alloy. Materials Research Letters. 2022;11(3):187-195.
37. Bian M, Huang X, Chino Y. Substantial improvement in cold formability of concentrated Mg–Al–Zn–Ca alloy sheets by high temperature final rolling. Acta Materialia. 2021;220:117328.
38. Zhu G, Wang L, Wang J, et al. Highly deformable Mg–Al–Ca alloy with Al2Ca precipitates. Acta Materialia. 2020;200:236-245.
39. Zhou B, Wang L, Jin P, et al. Revealing slip-induced extension twinning behaviors dominated by micro deformation in a magnesium alloy. International Journal of Plasticity. 2020;128:102669.
40. Jiang S, Jia Y, Wang X. In-situ analysis of slip transfer and heterogeneous deformation in tension of Mg-5.4Gd-1.8Y-1.5Zn alloy. Journal of Magnesium and Alloys. 2020;8(4):1186-1197.
41. Shi DF, Pérez-Prado MT, Cepeda-Jiménez CM. Effect of solutes on strength and ductility of Mg alloys. Acta Materialia. 2019;180:218-230.
42. Boehlert CJ, Chen Z, Gutiérrez-Urrutia I, et al. In situ analysis of the tensile and tensile-creep deformation mechanisms in rolled AZ31. Acta Materialia. 2012;60(4):1889-1904.
43. Bridier F, Villechaise P, Mendez J. Analysis of the different slip systems activated by tension in a α/β titanium alloy in relation with local crystallographic orientation. Acta Materialia. 2005;53(3):555-567.
44. Yaghoobi M, Ganesan S, Sundar S, et al. PRISMS-Plasticity: An open-source crystal plasticity finite element software. Computational Materials Science. 2019;169:109078.
45. Zhang C, Liu S, Zhang J, et al. Trifunctional nanoprecipitates ductilize and toughen a strong laminated metastable titanium alloy. Nat Commun. 2023 Mar 13;14(1):1397.
46. Zhang CL, Bao XY, Zhang DD, et al. Achieving superior strength-ductility balance in a novel heterostructured strong metastable β-Ti alloy. International Journal of Plasticity. 2021;147:103126.
47. Yang JK, Zhang CL, Zhang H, et al. Spinodal decomposition-mediated multi-architectured α precipitates making a metastable β-Ti alloy ultra-strong and ductile. Journal of Materials Science & Technology. 2024;191:106-121.
48. Wang L, Yang Y, Eisenlohr P, et al. Twin Nucleation by Slip Transfer across Grain Boundaries in Commercial Purity Titanium. Metallurgical and Materials Transactions A. 2009;41(2):421-430.
49. Bieler TR, Eisenlohr P, Zhang C, et al. Grain boundaries and interfaces in slip transfer. Current Opinion in Solid State and Materials Science. 2014;18(4):212-226.
50. Luster J, Morris M. Compatibility of deformation in two-phase Ti-Al alloys: Dependence on microstructure and orientation relationships. Metallurgical and Materials Transactions A. 1995;26:1745-1756.
51. Guo Y, Britton TB, Wilkinson AJ. Slip band–grain boundary interactions in commercial-purity titanium. Acta Materialia. 2014;76:1-12.
52. Bayerschen E, McBride AT, Reddy BD, et al. Review on slip transmission criteria in experiments and crystal plasticity models. Journal of Materials Science. 2015;51(5):2243-2258.
53. Xu J, Guan B, Xin Y, et al. The mechanism for Li-addition induced homogeneous deformation in Mg-4.5wt.% Li alloy. International Journal of Plasticity. 2023;170:103763.

Figures with captions

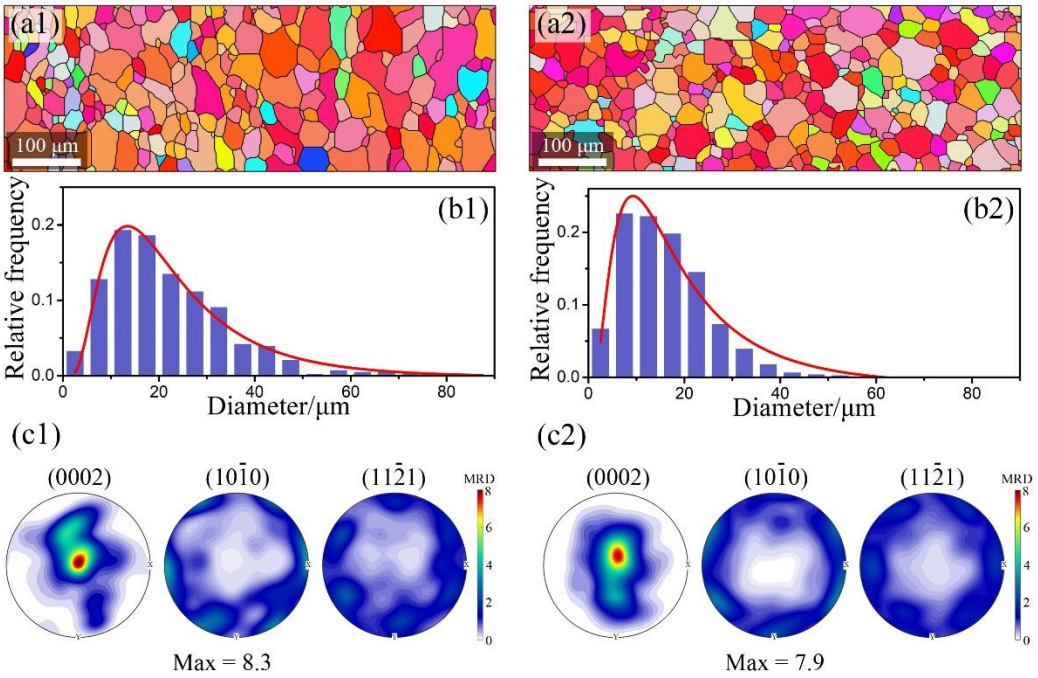

Fig. 1 The microstructure of the cold rolled and annealed Ti and HCP-MPEA: (a) ND-IPF maps; (b) Grain size distribution; (c) $\{0002\}$, $\{10\bar{1}0\}$, and $\{11\bar{2}1\}$ pole figures. Labels 1 and 2 denote pure Ti and HCP-MPEA, respectively. Note that the analyses for grain size distribution and pole figures were conducted using EBSD scans covering a broader area (Fig. S3) than depicted in the ND-IPF maps of (a)

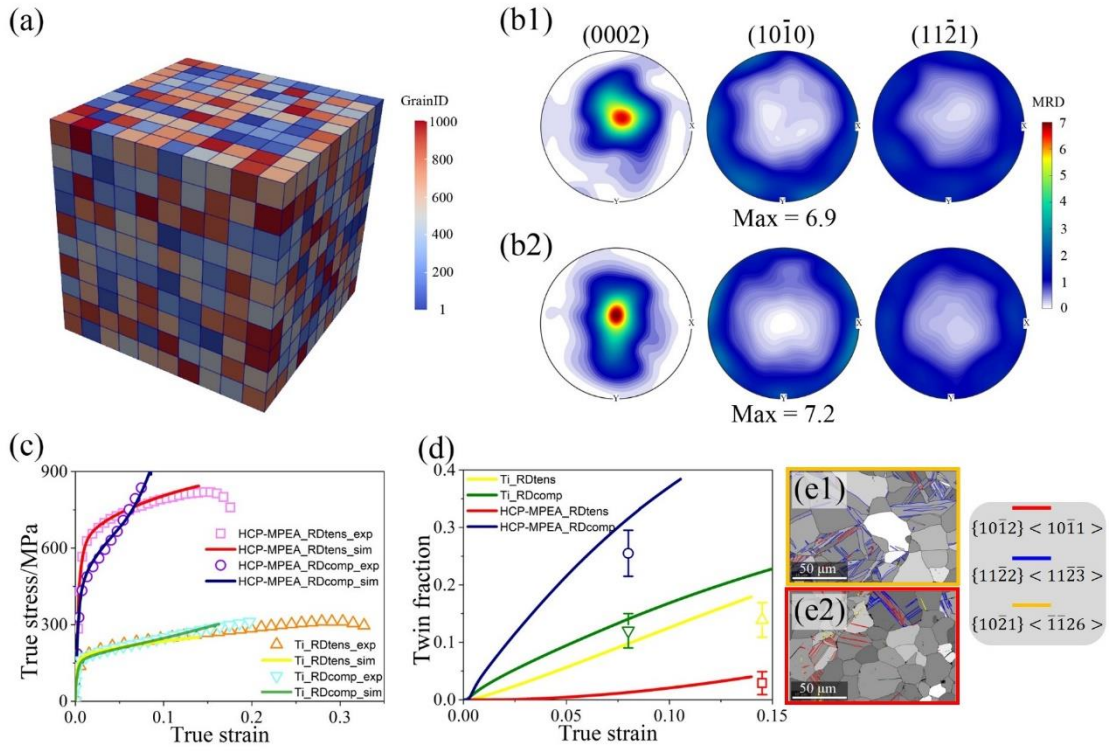

Fig. 2 CPFE modeling to capture the macroscopic mechanical response and microstructure and texture evolution: (a) the aggregate of 1000 single crystals used in the CPFEM; (b) initial textures used for CPFEM; (c) comparison of stress-strain curves from experiments and simulations; (d) comparison of twin volume fraction evolution; (e) microstructural representation of Ti and HCP-MPEA post-deformation at a true strain of ~0.15, highlighting twin boundaries.. Labels 1 and 2 in (b) and (e) indicate Ti and HCP-MPEA, respectively. Note that the compression tests were halted prior to specimen failure due to limitations of the testing equipment.

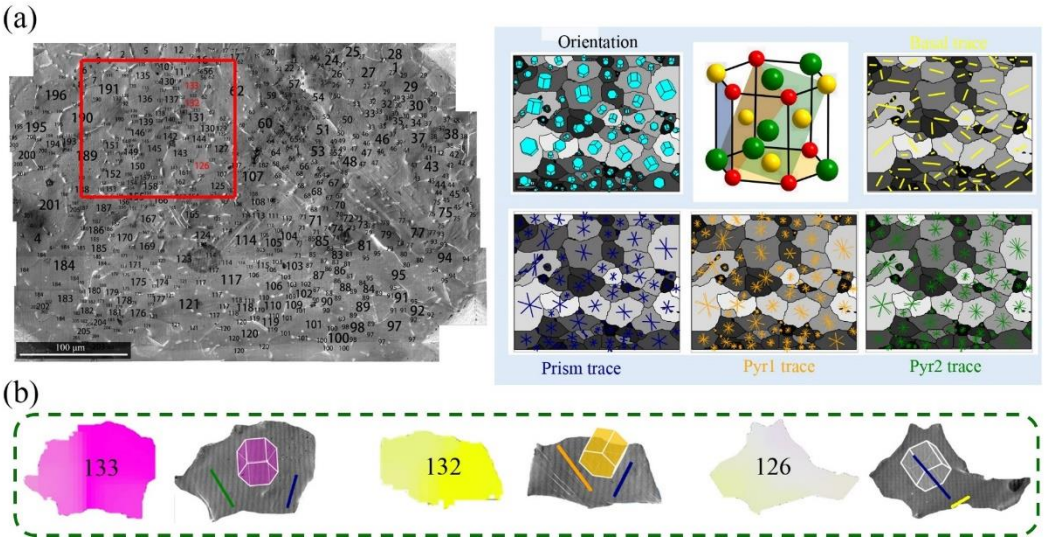

Fig. 3 One example of the present large-area high-resolution quasi-in-situ slip trace analysis: (a) a representative area observed under SEM alongside theoretical slip traces for various slip modes; (b) grain-by-grain high-resolution slip trace analysis uncovering very fine slip traces. The yellow, navy, orange, and olive lines represent Basal, Prism, Pyr1, and Pyr2 slip traces, respectively.

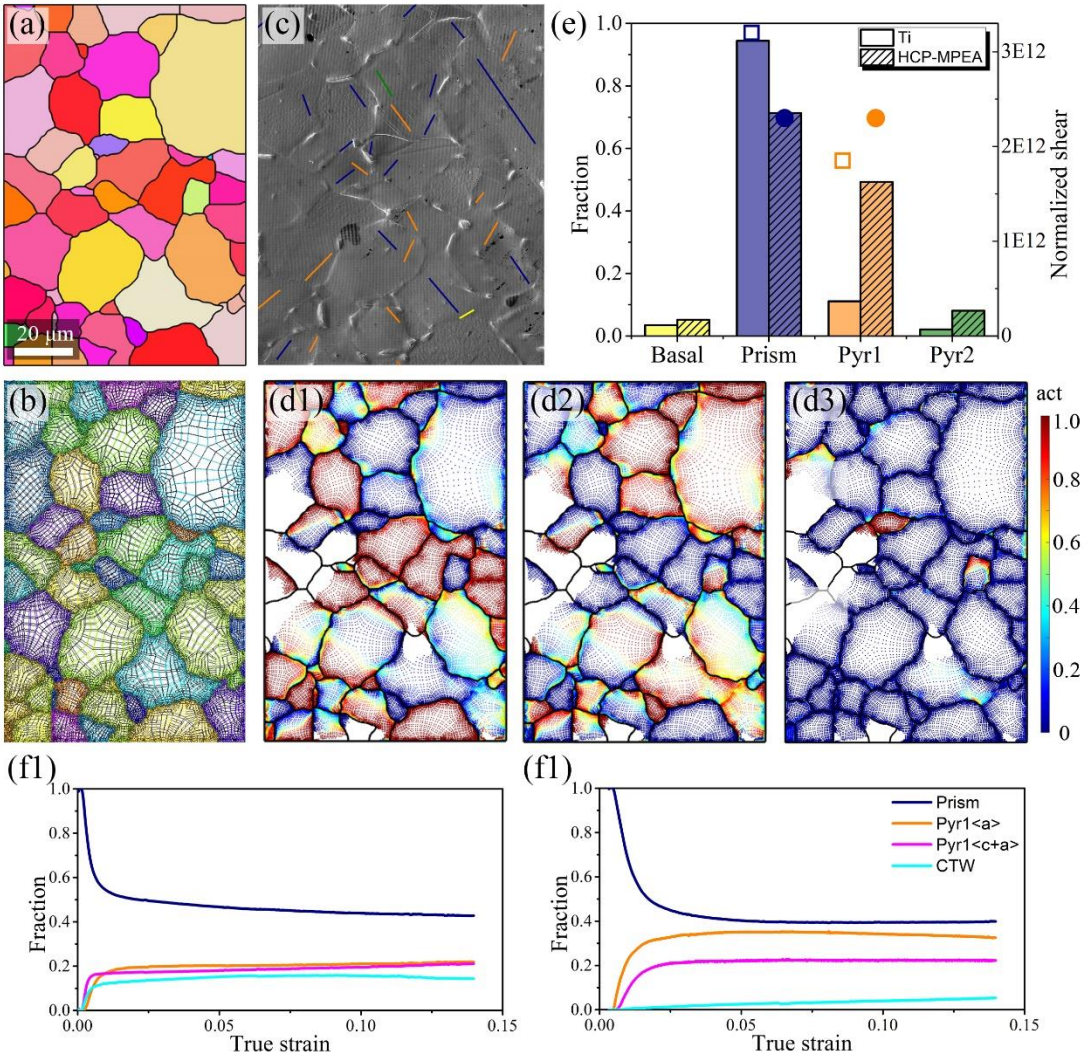

Fig. 4 Slip activity analysis: (a) a representative region in HCP-MPEA before tension; (b) FE mesh generated for the area shown in (a), used as input for CPFEM; (c) SEM image showing surface morphology of the same area as (a) after applying a true plastic strain of ~0.08; (d) CPFEM-predicted slip activity distribution; (e) experimental slip trace statistics alongside the normailzed shear on different slip planes predicted by CPFEM; (f) Variation of slip activity with strain. In (d), labels 1, 2, and 3 indicate Prism<a>, Pyr1<a>, and Pyr1<c+a> slip systems, respectively. In (f), labels 1 and 2 denote the data for Ti and HCP-MPEA, respectively. The bars indicate experimental data, while the scatter symbols represent normalized shear values derived from CPFEM. Empty symbols and unpatterned bars correspond to Ti, while solid symbols and patterned bars denote HCP-MPEA. Distinct colors differentiate the various slip planes.

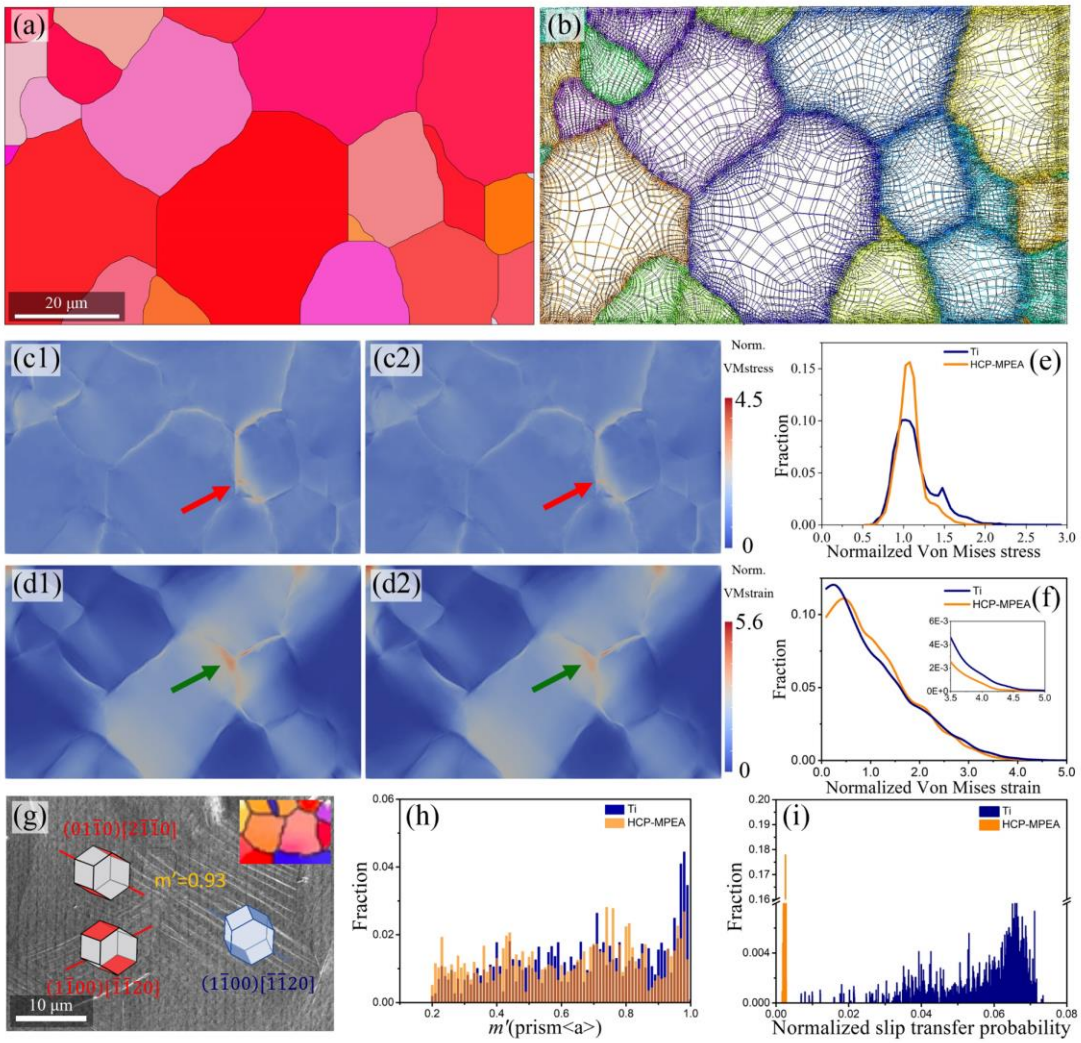

Fig. 5 Mesoscale stress/strain distribution: (a) ND-IPF map of a typical virtual microstructures before tension; (b) the FE mesh generated according to (a); (c) map of normalized Von Mises stress; (d) map of normalized Von Mises strain; (e) statistical distribution of normalized Von Mises stress; (f) statistical distribution of normalized Von Mises strain; (g) one representative region showing slip transfer in Ti; (h) statistical distribution of m'; (i) statistical distribution of slip transfer probability. Labels 1 and 2 in (c) and (d) denote Ti and HCP-MPEA, respectively.